FISEVIER

Contents lists available at ScienceDirect

Journal of Materials Science & Technology

journal homepage: www.elsevier.com/locate/jmst



Research Article

Reinforcing carbonized polyacrylonitrile fibers with nanoscale graphitic interface-layers



Rahul Franklin^{a,1}, Weiheng Xu^{b,1}, Dharneedar Ravichandran^b, Sayli Jambhulkar^b, Yuxiang Zhu^b, Kenan Song^{c,*}

- a Materials Science and Engineering, School for Engineering of Matter, Transport and Energy, Arizona State University, Tempe, AZ 85287, United States
- b System Engineering, The Polytechnic School (TPS), Ira A. Fulton Schools of Engineering, Arizona State University, Mesa, AZ 85212, United States
- ^c Manufacturing Engineering, Arizona State University, 6075 Innovation Way W., Mesa, AZ 85212, United States

ARTICLE INFO

Article history: Received 2 January 2021 Revised 24 March 2021 Accepted 27 March 2021 Available online 24 May 2021

Keywords: Mechanical property Graphene Nanocomposite Multilayer Electrical Sensing

ABSTRACT

Carbon fibers going through stabilization, carbonization, and graphitization heat-treatment stages will form continuous graphitic layers that are closely packed and preferentially aligned along the fiber axis, forming high mechanical stiffness or strength and electrical or thermal conductivity. The alignment of noncontinuous, powder-like graphene layers in polymers has been challenging due to the low bending modulus of a few- or even single-layered graphene, which causes aggregations or folding behaviors. This research demonstrates the leveraging of polymer-nanoparticle interactions to align graphene nanoplatelets (GNPs) in the polyacrylonitrile (PAN) matrix. An in-house designed spinning method produces a three-layered fiber that utilizes the interfacial interactions between each layer for graphene alignment between graphitic layers. This composite containing oriented GNPs significantly improves modulus (i.e., 42.3 to 74.6 GPa) and increases electrical conductivity for enhancing volatile organic compounds (VOCs) sensing behaviors. This research opens up a new scalable fabrication method for multilayered composites.

 $\ensuremath{\mathbb{C}}$ 2021 Published by Elsevier Ltd on behalf of Chinese Society for Metals.

1. Introduction

Current carbon fibers (CFs) are from carbonized precursors, e.g., cellulose, lignin, pitch, polyacrylonitrile (PAN), or Kevlar [1–3]. The current state-of-the-art in carbon fiber manufacturing has been the studies of processing parameters, including atmosphere effects [1], precursor type influences (viscose rayon fibers [4], PAN fibers [5], and isotropic pitch [6]), and material sustainability (precursors from cellulose or lignin [7]).

As compared to pitch, PAN has advantages of controlled molecular weights from chemical synthesis, easy processability, and reduced viscosity due to solubility in a variety of solvents, and controlled crystallinity and molecular alignment that can benefit the efficiency of carbon fiber conversion [8,9]. There are three stages in the transformation of precursor PAN fibers to CFs [10,11]:

(a) Oxidative stabilization (i.e., an oxidative atmosphere, 200–300 °C, with or without tension, hours) produces oxidized ladder

E-mail address: kenan.song@asu.edu (K. Song).

polymer parallel to the fiber axis by the cyclization of the pendant nitrile groups and the incorporation of oxygen.

- (b) Carbonization (i.e., a nitrogen atmosphere, 400–1500 °C, with or without applied tension) removes non-carbon elements as violative products, e.g., HCN, NH₃, N₂, H₂O, CO₂, CH₄, and H₂. The yielded CFs have around 50% of the original fiber mass. Observed are the phenomena of end-to-end joining of cyclized regions, aromatization of non-cyclized regions, and side-by-side condensation reactions between laddered structures to result in broader heterocyclic regions. Dehydrogenation and denitrogenation occur at a temperature of 1000 °C, giving rise to carbon ribbons containing limited N mass. The increased perfection of the carbon layer-plane packing is enhanced with increased temperature treatments.
- (c) Graphitization (i.e., an inert atmosphere, above 2000 °C, with applied tension) generates graphene structures. PAN-based fibers are turbostratic graphite even after graphitization, mainly because the helical crystal structure lacks a definite crystallographic arrangement of layer planes in terms of 3D stacking. Even at a high temperature of 2500 °C in argon, graphitization treatment will not generate the stacked graphene layers, as seen in pitch-based CFs. This lack of graphitic stacking is also why PAN-based fibers possess high strength due to graphitic

^{*} Corresponding author.

¹ These authors contributed equally to this work.

plane entanglement, while pitch-based fibers have high modulus due to close packing density and high graphitic plane orientations. The majority of current research suggests the structural benefits with tension in (a-c) procedures, while there have been efforts to investigate heat-treatments without tension or at lower temperatures for cost-efficient carbon fiber manufacturing [8,9].

With the incorporation of one-dimensional (1D) carbon nanotubes (CNTs) and carbon nanofibers (CNFs), PAN-based polymer fibers and their characteristics have been intensively studied [12]. Reported efficient reinforcing mechanisms are primarily attributed to strong filler-matrix interfacial interactions and good dispersion quality and CNT-induced polymer self-assembly with ordering, which in turn enhances interfacial properties [13-15]. Groups from Kumar [16], Naraghi [17], Espinosa [18], Dzenis [19], and Minus [20] have provided numerous examples. Such composites with low CNT loading (typically less than 5 wt%) can be produced by solution or melt processing and in-situ polymerization. Two-dimensional (2D) graphene, as the allotrope of CNT, has similar high intrinsic properties, but in contrast, has been less frequently used in PAN-based fibers or carbon fiber reinforcement. The primary reason is the dilemma between maximized dispersion quality and optimized graphene morphologies [21]. For efficient mechanical and electrical enhancement, graphene needs to have high degrees of exfoliations and fewer layer numbers to be well-distributed in colloidal suspensions and subsequent polymer matrices. A recent paper from Duin, Zhigilei, and Li group has simulated the effects of including rather low concentrated graphene (0.075 wt%) on improving CFs modulus and strength [22]. The simulation has shown the benefits of single-layer graphene in facilitating carbonization and graphitic layer orientations. However, the bending modulus of graphene is proportional to cubed thickness $(t^3, t \text{ is the graphene thickness})$ [23], meaning that the integrity of graphene will significantly get lost as a function of decreased graphene layers. As a result, a few graphene layers will be crumpled or folded, serving as structural defects, causing crack initiation, and scattering electrons or phonons for negative property effects [24].

This work focused on the carbonization of PAN-precursor fibers and the feasibility examination of including graphitic layers for enhanced mechanical and functional properties in carbonized fibers. In this way, the carbonized fibers had hybrid structures between PAN- (i.e., turbostratic layers from PAN) and pitch-based (i.e., graphitic layers from GNPs) fibers. An efficient enhancement of fiber performance could also avoid high-temperature heattreatment and noticeably reduce carbon fiber manufacturing costs. Note that we utilized tension-free heat-treatment during stabilization and carbonization due to the low molecular weight PAN and low-quality GNP suspensions; as a result, we did not compete our CFs with commercialized ones (e.g., a strength 1-7 GPa and modulus 200-800 GPa) [25]. Instead, we emphasized a new manufacturing method that produced multilayered multifunctional composite fibers with precise interfacial engineering for graphene morphology control. We designed and 3D printed a unique spinneret with optimized structures and dimensions to embed graphitic layers in PAN-based fibers. The incorporation of polymers and carbon nanoparticles in separate phases induced coaxial layers to form along the fibers. The mechanical reinforcement before and after carbonization was investigated and the inclusion of 1 wt% GNPs showed higher mechanical properties than pure PAN fibers after carbonization. Due to their excellent mechanical and electrical properties, carbonized fibers also have broad applications in sensors, supercapacitors, actuators, and filtration devices [26-29]. Thus, this research also demonstrated our carbonized fibers' uses in sensors that were efficiently responsive to, for example, chemical gases and mechanical pressures.

2. Experimental

2. 1 materials

PAN copolymer (i.e., 99.5% acrylonitrile/ 0.5% methacrylate) with a molecular weight of 230,000 g/mol and a mean particle size of 50 μm was obtained from Goodfellow Cambridge Limited, Huntingdon, England. GNPs (i.e., surface area 120–150 m^2/g) were obtained from Sigma-Aldrich, US, and CNTs (i.e., NC 7000, with an average diameter of 9.5 nm, length of 1.5 μm , surface area of 250–300 m^2/g , 90% carbon purity, and volume resistivity measured on powder at $10^{-6}~\Omega/m$) were obtained from Nanocyl SA, Belgium. High-resolution scanning electron microscopy (SEM) images of the as-obtained GNPs and CNTs are shown in Fig. 1. N, N-Dimethylformamide (DMF, ACS reagent, \geq 99.8%) as the polymersolvent and methanol (ACS reagent, \geq 99.8%) as the coagulant were obtained from Sigma-Aldrich, US. All materials were purchased and used as received without further modifications.

2.2. Manufacturing processes of fiber spinning and heat-treatment

Table 1 lists the terminology for manufactured fibers and their manufacturing details. The following sections described the preparation of the spinning procedures for three types of fibers. 1-phase PAN fibers: A 15 wt% PAN/DMF solution was made by dissolving 22.5 g PAN in 150 mL DMF at 85 °C under a mechanical stir for 2 h until obtaining a transparent solution. The solution was then deaerated in a vacuum oven (Lindberg Blue M lab oven, Thermo Scientific, US) for 1 h. The bubble-free solution was carefully transferred to a metal syringe connected to a syringe pump for fiber spinning at an injection rate of 2 mL/min.

D-phase PAN-nanoparticle composite fibers: A dispersion of GNP/DMF was first obtained through 20 min of tip sonication at 60% amplitude (Q500, Fisherbrand, US). The dispersion was added to the prepared PAN/DMF solution to obtain different GNP concentrations (i.e., 1 wt% and 10 wt%) followed by 2 h of stirring at 85 °C. The mixture was then transferred to a metal syringe for fiber spinning at an injection rate of 2 mL/min.

3-layered PAN/PAN-nanoparticle/PAN composite fibers: 3layered fibers consisted of coaxial stacking layers (black, red, and blue colors in Fig. 2). The spinneret has three channels responsible for generating the interior, middle, and exterior layers, each of which was fed by one type of spinning dope. Composition-wise, both the inner and outer layers were filled with 15 wt% PAN/DMF solutions with the same preparation procedures for the abovementioned 1-phase PAN fibers. The composition of the middle layer varied based on the weight of polymers and nanoparticles added. The concentrations of PAN/DMF were 0 wt%, 5 wt%, 10 wt%, and 15 wt%. Both GNP/DMF and CNT/DMF suspensions were added to the pre-dissolved PAN/DMF solutions in a manner similar to that for the D-phase spinning dope, and they were labeled, as shown in Table 1. The syringe pump's injection rates were 1 mL/min for the middle channel and 2 mL/min for the interior and exterior channels.

Fiber spinning: Dry-jet wet-spinning was used to fabricate both the pure PAN and the PAN/nanoparticle composite fibers (Fig. 2). The in-house developed 3-layered spinneret was critical in positioning/placing polymers and nanoparticles at different layers. An air gap of 2 cm was chosen for sufficient polymer chain extension, crystallization, and alignment before forming gels with physically crosslinked macromolecules. The gel fibers underwent DMF/methanol solvent exchange for increased stiffness so that they could be collected on fiber winders. The take-up

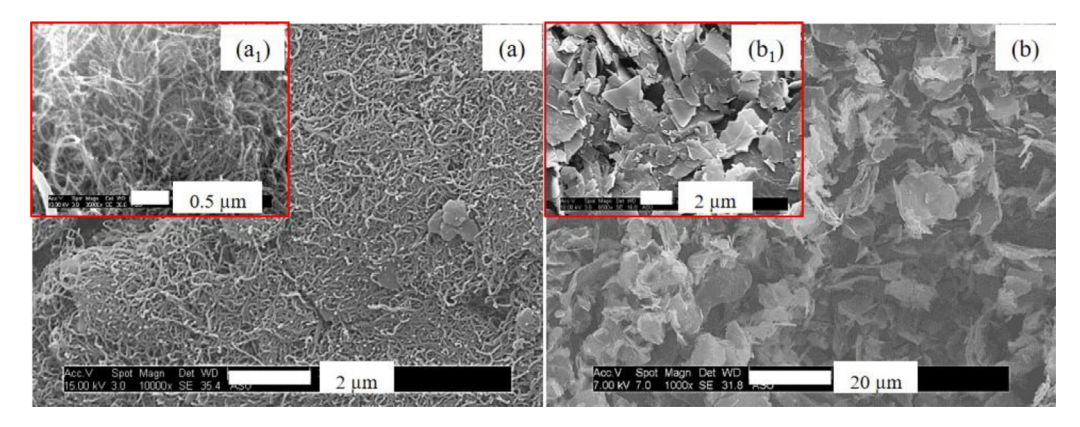


Fig. 1. SEM images of as-obtained CNTs (a) and GNPs (b) with the magnified images of both materials (a₁, b₁).

Table 1 Summary of fiber terminology, compositions, processability, and testability.

Fiber type	Fiber name	Compositions (wt%)				Processability and testability		
		Interior and exterior layers	Middle l	ayer		Coinnabilitu#	Hart traction of the	Mechanical
		PAN/DMF (wt%)		GNP	CNT	Spinnability#	Heat-treatment *	testability+
1-phase	15%PAN	15	N/A	N/A	N/A	Y	Hot drawing at	Y
D-phase	15%PAN/1%GNP-D	15	N/A	1	N/A	Y	110, 130, and	N
3-Layered	0%PAN/10%GNP-3	15	0	10	0	Y	150 °C;	N
	5%PAN/10%GNP-3		5	10	0	Y	stabilization at	N
	10%PAN/10%GNP-3		10	10	0	Y	280 °C for 1.5 h,	N
	15%PAN/10%GNP-3		15	10	0	N	carbonization at	Y
	15%PAN/1%GNP-3		15	1	0	Y	1250 °C for 10	Y
	15%PAN/1%CNT-3		15	0	1	Y	min	Y

- # Spinnability showing a too high viscosity of composition 15wt%PAN/10wt%GNP to spin fibers, with a spinnability of N; Y, spinnable; N, not spinnable.
- * All carbonized fibers have the designation 'HT' placed before the established terminology (e.g., HT-15%PAN), meaning the 15%PAN fibers were treated after hot drawing, stabilization, and carbonization.
 - $^+$ Feasibility of handing carbonized fibers during mechanical tests. Y= Yes; N= No.

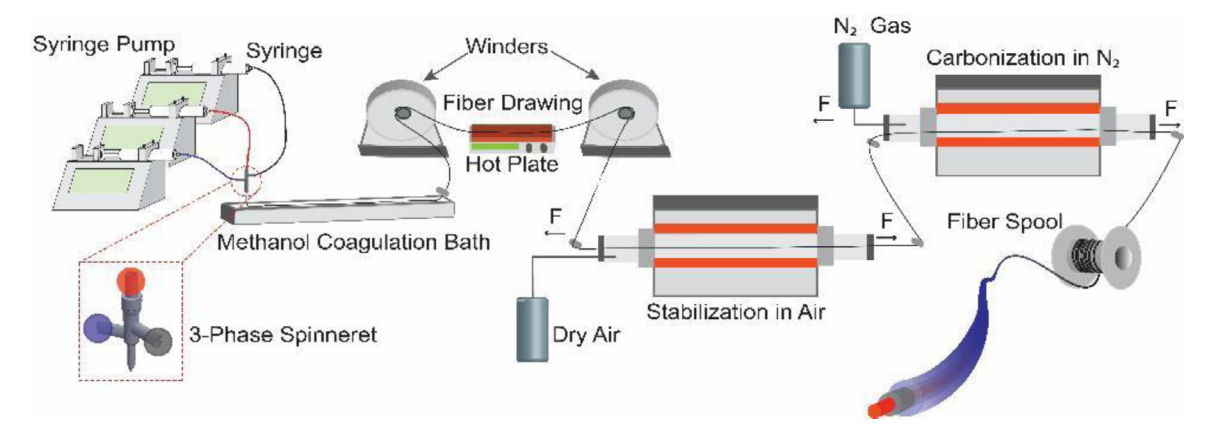


Fig. 2. Manufacturing of 3-layered composite fibers and post-treatment at three stages (drawing, stabilization, and carbonization) (For interpretation of the references to color in this figure, the reader is referred to the web version of this article.).

speeds of different fibers, varied due to their rheological behaviors, were chosen at the highest rate without losing continuity. These fibers were drawn at temperatures of 110 °C, 130 °C, and 150 °C, consecutively for a maximized molecular extension, and the corresponding draw ratios are listed in Table S1 in the Supporting Information. All fibers were stabilized at 280 °C and carbonized at 1250 °C, according to Fig. S1 in the Supporting Information. Applying tensions (e.g., ranging from 3 to 10 MPa, based on our setup (Fig. S1 in the Supporting Information)) was not successful, which was likely due to the higher defect den-

sity from larger fiber diameters and the GNP-induced crack propagation before fibers were fully carbonized/graphitized. As a result, fibers were heated by wrapping around an alumina boat. Notice that the final fibers of 15%PAN, 15%PAN/1%GNP-3, and 15%PAN/1%CNT-3 were studied regarding their properties only because other fibers were too brittle to be tested or further processed (Table 1). However, the study of other fibers, especially the morphologies of the 3-layered fibers with different polymer concentrations in the middle layers, is essential in understanding the polymer-nanoparticle interactions as a function of their

configurations and interfacial engineering for high-performance composites.

2.3. Characterization

Differential Scanning Calorimetry (DSC) (DSC 250, TA Instruments Inc., USA) was conducted on 3 mg fiber samples with different heating rates to 350 °C in a nitrogen atmosphere to understand the cyclization behaviors, followed by reruns in the air for oxidation and crosslinking studies. Single filament tensile tests were conducted using a tensile tester (Discovery HR-2 hybrid rheometer, TA Instruments Inc., USA). A constant linear strain rate of 150 µm/s and a gauge length of 5 cm was used for the pre-carbonized fibers and a constant linear strain rate of 50 µm/s and a gauge length of 1 cm was used for carbonized fibers. A number of 5-10 samples were tested for the mechanical parameters. SEM (XL-30 Environmental SEM, Philips, NL) was used to characterize fiber morphology at an operating voltage of 10 kV. All fibers were fractured in liquid nitrogen and mounted on a 90° pin stub with the fractured end facing up for SEM imaging. All SEM samples were coated with a thin gold/palladium layer (15-20 nm) for image analysis of surface morphology, voids, and interfacial interactions. Electrical resistivity measurements of the pre- & post-heat-treated fibers were tested using a multimeter (DMM 7510, Keithley, US). The resistivity as a function of chemical gases or mechanical pressures was monitored for sensing applications with an in-house designed setup [30].

3. Result and discussion

3.1. Fiber draw ratios

After collecting via fiber winding, all the PAN and composite fibers were hot-drawn to maximize the polymer chain extension. The purpose of this hot-stage drawing was for better graphitic plane packing and orientations during the post-spinning (i.e., stabilization, carbonization, and graphitization) of CFs. The draw ratio of pure PAN fibers was 8.0, and a 1 wt% GNPs inclusion increased this value to 9.6 in the composites, which is consistent with our previous studies of lubrication effects caused by graphene or similar nanoparticle layer exfoliations [9,31]. The presence of 10 wt% GNPs in the middle layer significantly decreased the drawability to 6.7, and through adding PAN of 5 wt% and 10 wt% in the middle layer, the draw ratios increased to 11.6 and 8.0, respectively. However, a mixture of 15 wt% PAN and 10 wt% GNP in the middle layer (i.e., 15%PAN/10%GNP-3) was not spinnable at the 2 cm airgap due to its low viscoelastic behavior (Table 1). The drawn fibers also showed a consistent decrease in fiber diameters after the three-stage hot-drawing, namely, 191.4 µm for 0%PAN, 114.0 µm for 5%PAN, and 65.7 µm for 10%PAN in 10%GNP (Table S1 in the Supporting Information). The 15%PAN/1%GNP-3 and 15%PAN/1%CNT-3 composite fibers showed the same diameters, i.e., 77.80 µm, much smaller than both 1-phase and D-phase fibers.

3.2. Kinetic analysis

Different concentrations of PAN polymer in the middle layer resulted in different draw ratios and fiber diameters, all related to the structural properties of the 3-layered fibers. To better understand these variations and their influence on the thermal treatment before carbonization, selected PAN and composite fibers (i.e., 15%PAN, 0%PAN/10%GNP-3, and 10%PAN/10%GNP-3 fibers) were analyzed. Thermal stabilization is a critical stage for PAN-based carbon fiber fabrication that affects PAN polymer chain transformation into stabilized ladder structure through a series of (i.e., oxidation, cyclization, and crosslinking) reactions. Since oxygen is mandatory

 Table 2

 Activation energies determined from the Kissinger method (kJ/mol).

	15%PAN	0%PAN/10%GNP-3	10%PAN/10%GNP-3
Cyclization	146.5	151.8	144.5
Oxidation	84.2	77.5	88.4
Crosslinking	138.5	112.1	132.4

for the oxidation and crosslinking process, a separate monitoring strategy was used as the fibers were first run under nitrogen atmosphere to study the cyclization process, followed by a rerun in the air to study the oxidation and crosslinking behaviors in the DSC. During these processes, different heating rates were used to study the kinetics and the associated activation energies. The single peak in the nitrogen atmosphere corresponds to the cyclization process (Fig. 3(a-c)), and the two peaks in their corresponding reruns in the air represent the oxidation and crosslinking processes (Fig. 3(d-f)) [32]. The peak temperatures (T) of cyclization, oxidation, and crosslinking are listed in Table S2 in the Supporting Information and the activation energy values were obtained by the fitting based on the Kissinger equation (Eq. (1)) [33]:

$$-\frac{E_{a}}{R} = \frac{d\left[\ln\left(\frac{\varphi}{T^{2}}\right)\right]}{d\left(\frac{1}{T}\right)} \tag{1}$$

where E_a is the activation energy (kJ/mol), φ is the heating rate (°C/min), R is the molar gas constant [33]. E_a was taken as the slope of the plots of $\ln(\varphi/T_m^2)$ versus $1/T_m$ in Fig. 3(g-i) and is summarized in Table 2.

The cyclization activation energies were not significantly affected with additional GNPs in the middle layer, which is consistent with previous work [34]. However, the activation energies for oxidation and crosslinking of the 0%PAN/10%GNP-3 fiber showed much lower values than the 15%PAN and 1-%PAN/10%GNP-3 fibers. Since oxidation and crosslinking require an oxidative environment to proceed, one explanation was the faster oxygen diffusion in the middle layer, indicating a void-containing structure [35]. As the 0%PAN/10%GNP-3 fiber contained only GNPs and DMF in its middle layer, voids were likely to be formed during the solvent-induced phase change process during the fiber spinning. Eventually, these voids led to defects during the drawing procedure, resulting in the lower draw ratio of the 0%PAN/10%GNP-3 fiber.

On the contrary, the 10%PAN/10%GNP-3 fibers had similar activation energies to the pure PAN fibers, indicating a denser structure for higher PAN concentration in the middle layer than the 0%PAN/10%GNP-3 fibers. PAN polymers filled the defects in the middle layer and improved its interfacial interactions with interior and exterior PAN layers. Lower E_a indicating a more oxygen permeable structure may benefit in lowering the energy consumption during the stabilization procedure [36] as occurred in 0%PAN/10%GNP-3 fibers, the chunked nanoparticles resulted in uncollectable fibers after the carbonization procedure. Realizing that lower GNP loading for lubrication effects and higher PAN concentrations would generate better macromolecular drawability and structural perfections, 15%PAN/1%GNP-3 and 15%PAN/1% CNT-3 fibers were examined for their reinforcement efficiencies.

3.3. SEM characterization

Fig. 4 shows the cross-sectional SEM images of all 3-layered fibers as a function of increased PAN/GNP ratios in the middle layers. Both 0%PAN/10%GNP-3 and 5%PAN/10%GNP-3 fibers showed prominent void spaces in the middle layer before and after carbonization, which led to the higher oxidation efficiency as reported from DSC results (Fig. $4(a_1-a_3)$ and Fig. $4(b_1-b_3)$). An increase in PAN concentration led to a more compact GNP morphology in the

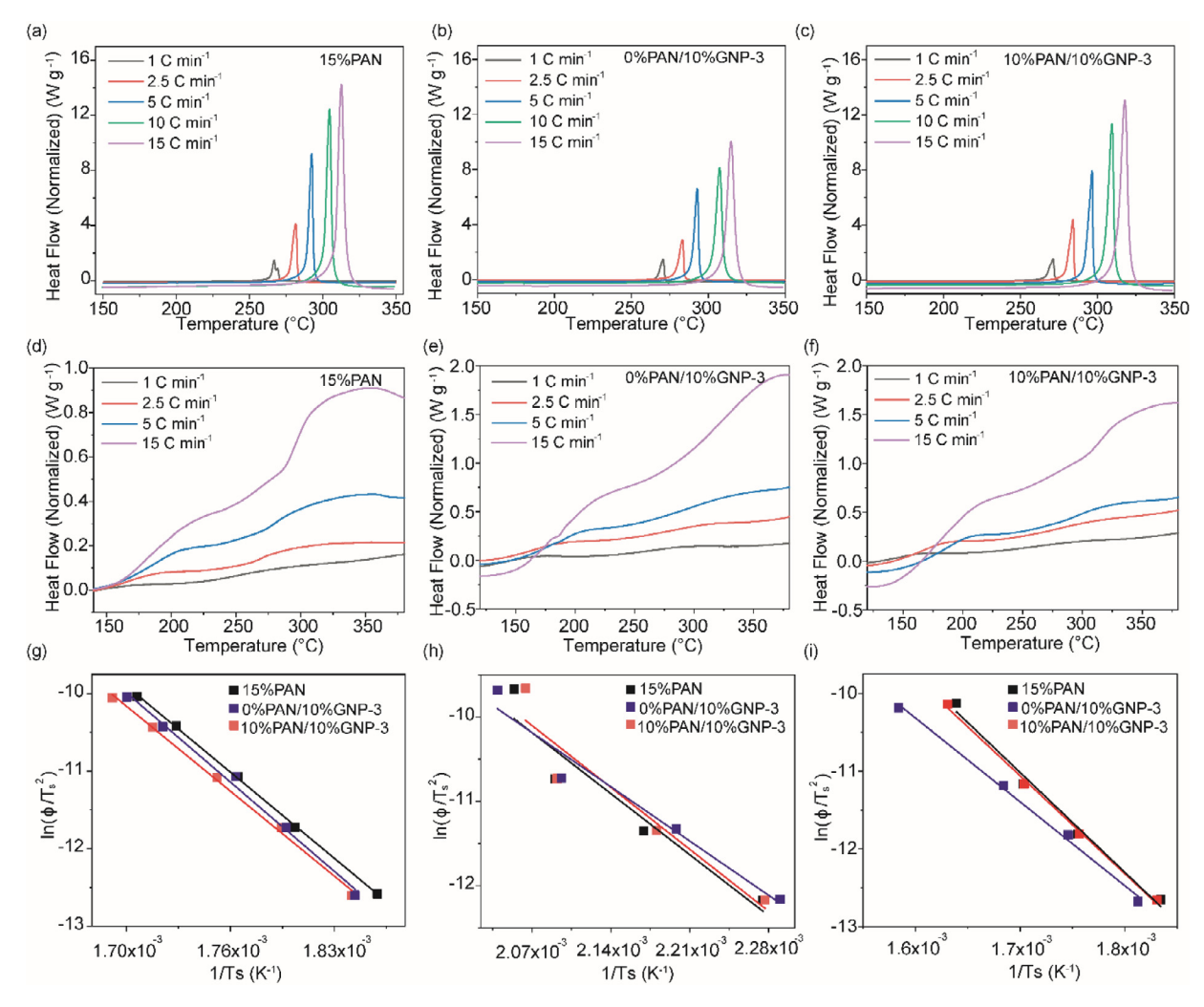


Fig. 3. DSC curves of different heating rates for (a) 15%PAN, (b) 0%PAN/10%GNP-3, and (c) 10%PAN/10%GNP-3 fibers in nitrogen, followed by their corresponding re-runs in the air (d), (e), and (f). Plots of $\ln(\varphi/T_m^2)$ versus $1/T_m$ according to the Kissinger method for activation energies of (g) cyclization, (h) oxidation, and (i) crosslinking reactions [33].

middle layer (i.e., 0% vs. 5% vs. 10%PAN/10%GNP in Fig. $4(c_1-c_3)$). The relative PAN/GNP content in the middle layer also significantly affected the GNP morphologies, resulting in preferentially aligned GNPs, as observed in each of the zoomed-in sections (Fig. 4(a₃c₃)). The layered and porous structure in the 0%PAN/10%GNP-3 fibers was due to the permeation rate variations determined in the spinning process. When thicker and denser PAN outside the GNP channel formed gels on fiber surfaces during coagulation, the permeation rates slowed down towards the fiber core due to the less accessibility to PAN materials in the middle layer (e.g., 5 wt%PAN < 10 wt%PAN < 15 wt% PAN in Fig. $4(a_1-c_1)$). As a result, the less involvement of PAN in the middle layer led to more porous structures. A high concentration of PAN (e.g., 15 wt%) and low concentration of GNPs (e.g., 1 wt%), instead, had similar gelation kinetics to the PAN in the most interior and exterior layers, resulting in densified microstructures without micropores (Fig. $4(d_1-d_3)$). A similar structure could be observed for high PAN concentrations in the 15%PAN and 15%PAN/1%CNT-3 fibers (Fig. S2 in the Supporting Information).

On the other hand, SEM images for the D-phase fiber (15%PAN/1%GNP-D) suggested the formation of large GNP aggregates throughout the fiber (Fig. S3 in the Supporting Information), resulting in the lower draw ratio, 9.6, compared to 12.2 of the 15%PAN/1%GNP-3 fiber. All 10% GNP-containing fibers exhibited graphitic middle layer structure after carbonization, resem-

bling other reported graphene-based fibers (Fig. $4(a_2-c_2)$) [37,38]. However, voids also appeared due to the different thermal degradation degrees between PAN polymer chains and the graphitic GNP nanoparticles. For 1% GNP-containing fibers, D-phase fiber showed much larger voids at the surface of the fractured cross-section (Fig. S3 in the Supporting Information) comparing to the 3-layered fiber (Fig. 4(d)), which could be the main cause for its low survivability during carbonization (Fig. S4 in the Supporting Information), resulting in a lack of feasibility for mechanical characterizations.

3.4. Mechanical analysis

The effect of increasing PAN concentration in the middle layer on mechanical properties was analyzed via tension tests. Before stabilization, the mechanical properties showed a significant increase with increasing PAN concentrations from 0% to 10% in the middle layer (Fig. 5(a)), as modulus increased from 1.3 GPa to 11.1 GPa and ultimate tensile strength increased from 39.8 MPa to 420.2 MPa (Table 3). The weakening of 0%PAN/10%GNP-3 and 5%PAN/10%GNP-3 fibers was primarily caused by the relatively fragile bonding (van der Waals forces) and sliding/exfoliating between graphene bundles. The stepwise breaking points of the outer and inner layers at the fracture strain of the 0%PAN/10%GNP-3 fiber also suggested weak interfacial interactions between the lay-

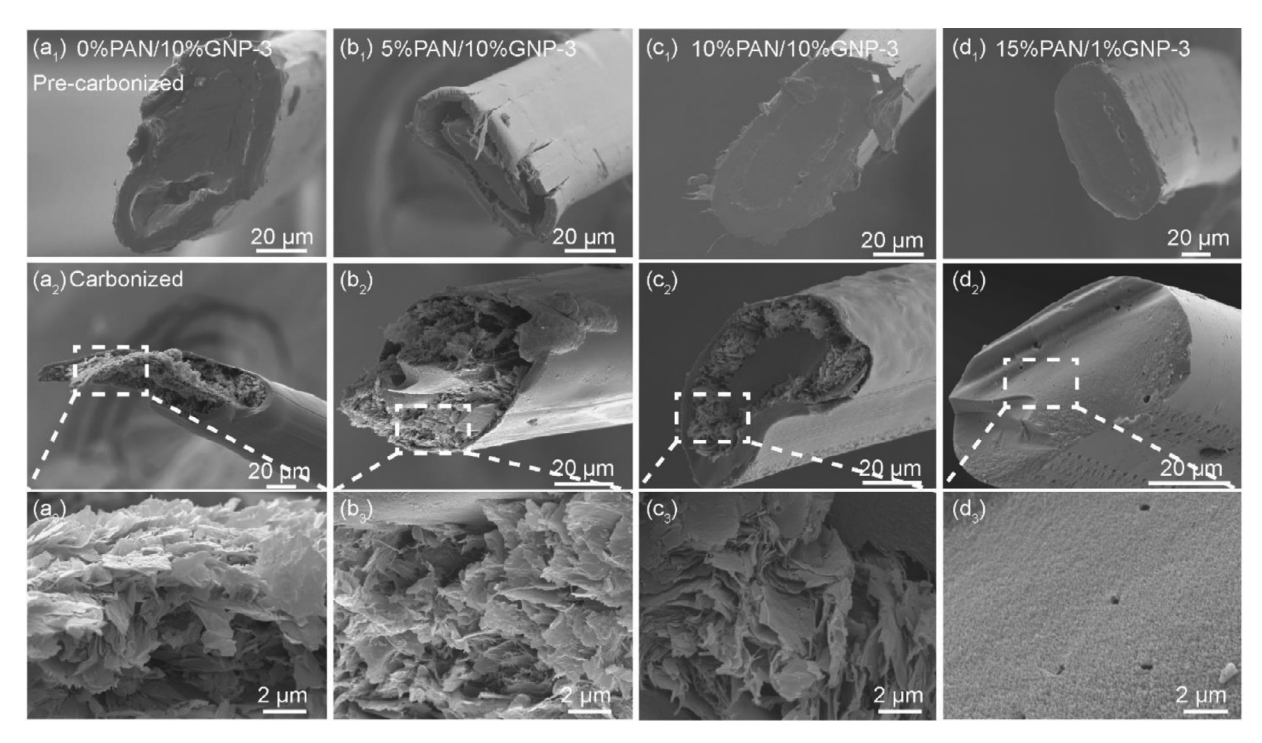


Fig. 4. Cross-sectional SEM images of the pre-carbonized and post-carbonized (a_1-a_3) 0%PAN/10%GNP-3, (b_1-b_3) 5%PAN/10%GNP-3, (c_1-c_3) 10%PNA/10%GNP-3, and (d_1-d_3) 15%PAN/1%GNP-3 fibers with zoomed-in sections on the middle carbonized GNP/PAN layer.

Table 3Mechanical properties before and after carbonization.

	Pre- stabilized fibers			Carbonized fibers			
	E (GPa)	σ (MPa)	ε (%)	E (GPa)	σ (MPa)	ε (%)	
15%PAN	9.3 ± 1.8	280.5 ± 44.6	8.1 ± 0.1	42.3 ± 11.4	320.4 ± 110.8	1.5 ± 0.5	
15%PAN/1%GNP-D	4.4 ± 0.8	190.2 ± 47.3	6.8 ± 6.2	Non-collectable after carbonization due to fiber			
0%PAN/10%GNP-3	1.3 ± 0.2	39.8 ± 5.1	8.4 ± 0.6	fracture in heat-treatment procedures (Fig. S4 in the			
5%PAN/10%GNP-3	4.5 ± 0.7	190.2 ± 26.9	10.2 ± 1.4	Supporting Information)			
10%PAN/10%GNP-3	11.1 ± 0.9	420.2 ± 30.1	8.2 ± 1.1				
15%PAN/1%GNP-3	9.0 ± 1.0	340.3 ± 25.7	9.4 ± 1.3	74.6 ± 17.6	440.2 ± 150.5	1.3 ± 0.6	
15%PAN/1%CNT-3	9.8 ± 1.5	320.4 ± 41.2	9.6 ± 1.0	38.9 ± 22.2	290.7 ± 140.4	1.1 ± 0.9	

ers (Fig. 5(a)). Furthermore, the higher porosity also led to higher defects and fractured points under tension.

Fig. 5(b) shows the comparison between various 1% nanoparticle-loaded composites and pure PAN fibers. The D-phase fiber showed a decrease in both Young's modulus and tensile strength from pure PAN (Table 3 and Fig. 5(b)). Theoretically, the addition of nanoparticle reinforcement should promote enhanced mechanical properties [39]. However, it is not uncommon to observe a deterioration effect with nanoparticle inclusion [40,41]. The low industrial-grade nanoparticle quality and poor sonication dispersion of GNPs can induce non-efficient load transfer at the nanoparticle-polymer interface. In contrast, under the same nanoparticle dispersing condition, 15%PAN/1%GNP-3 fiber showed a 105% and 78.9% increase in Young's modulus and ultimate tensile strength, respectively, as compared to the D-phase fiber. The enhanced reinforcement efficiency between the D-phase and 3layered fibers was most likely due to the layered structure through the 3D printed spinneret, as indicated in Fig. 5(c). During the fiber spinning procedure, the exterior PAN layer was in close contact with the hot plate, and polymer chains were stretched above the glass transition temperature. The extended polymer chains on the exterior layer (indicated in red) and the less extended polymer chains in the interior layer (indicated in blue) generated shear stress upon the middle layer, which contained graphene materials (indicated in black). This shear stress applied during the thinning

process slid the graphene layers little by little and simultaneously aligned the graphitic layers more to the fiber axis (Fig. 5(c)) [31,42]. The preferential alignment of 2D materials resulted in the anisotropic electron transport and stress transfer. Thus, high-performance multifunctional fibers were obtained. Notably, the middle layer's PAN content was also expected to serve as a constraint to the GNPs, maintaining their 2D geometry without folding and preserving planer alignment for efficient interfacial contacts. The preferential alignment of GNPs and CNTs are analyzed in the Section. 3.5.

To further investigate the reinforcement effects from GNP alignment and exfoliations and the nanoparticle orientation facilitation from PAN molecules, the fibers were heat-treated first at 280 °C for stabilization and then at 1250 °C for carbonization, as reported in many studies [43]. Raman spectroscopy was performed on the HT-10%PAN/10%GNP-3 fiber to demonstrate the carbonization efficiency across the fiber with the inclusion of the middle GNP-containing layer. Two points in the core layer and one point in the outer shell layer were chosen (Fig. S5 in the Supporting Information), and their associated Raman signature peak positions and full-width-at-half-maximums (FWHM) were identical, suggesting negligible differences in carbonization efficiency across layer thickness (Fig. S6 in the Supporting Information, fitted parameters in Table S3 in the Supporting Information) [25].

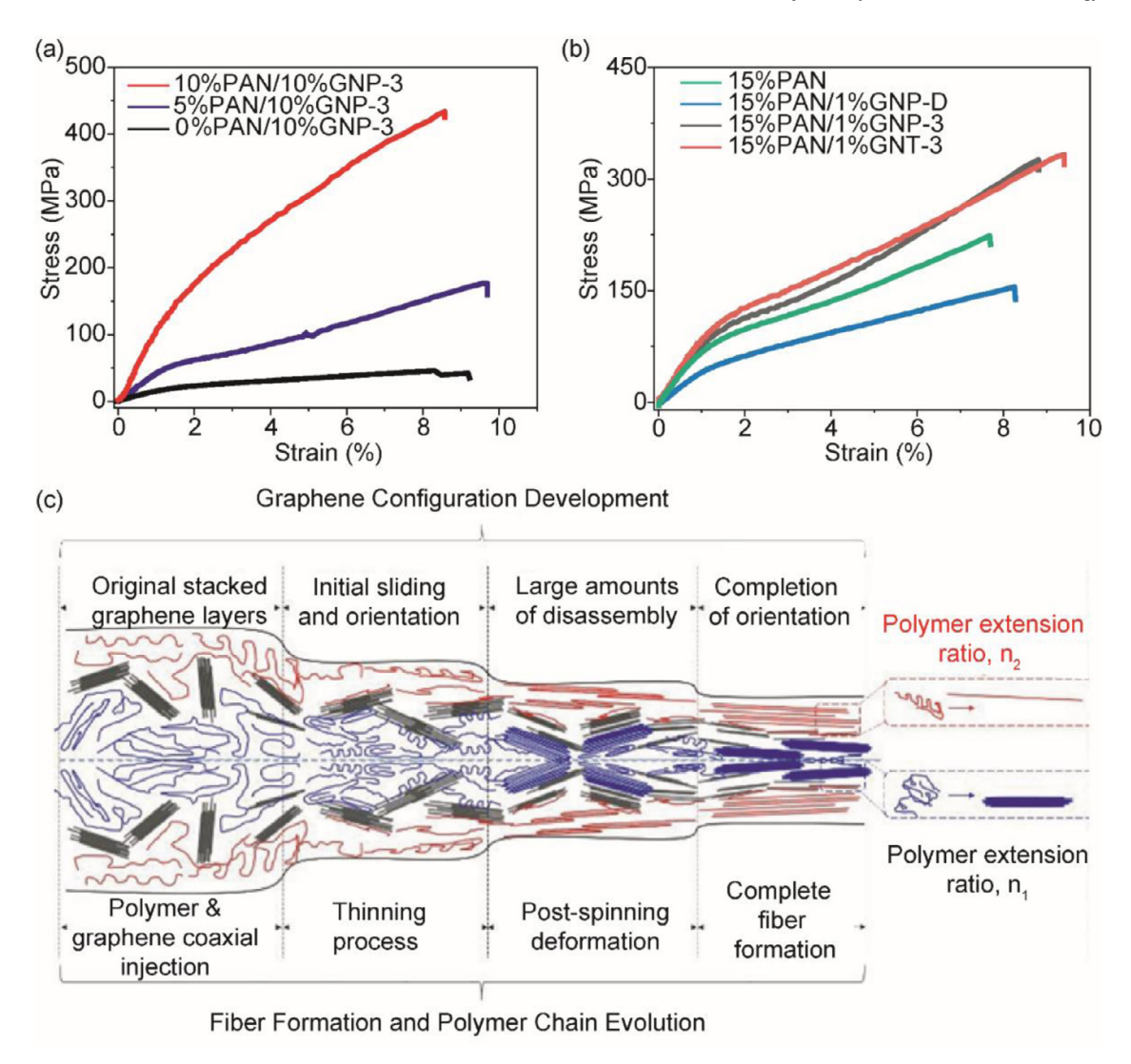


Fig. 5. Mechanical properties of the fibers prior to stabilization. (a) The effect of increasing PAN concentration in the middle layer. (b) Comparison between 15%PAN and 1 wt% nanoparticle loaded fibers with and without layered structures. (c) Schematic of the change in GNP orientation resulted from the relative molecular movements on internal (blue) and external (red) surfaces of graphene layers, resulting in aligned the GNPs in the fiber axial direction.

After carbonization, HT-15%PAN/1%GNP-3 fiber exhibited a 76% increase in modulus and 34% increase in strength compared to HT-15%PAN fiber (Table 3) with stress-strain curves shown in Fig. S7 in the Supporting Information. The enhanced mechanical properties showed the effectiveness of including PAN/GNP on mechanical reinforcement. However, the standard deviations for all carbonized fibers were high and mechanical data were more scattered than those fibers without defects (Table 3). Therefore, statistical analysis (i.e., Weibull analysis) was used to analyze propertydefect relationships, and a detailed procedure is shown in Fig. S8 in the Supporting Information [44,45]. Both the Weibull modulus and strength fitted values are listed in Table S4. Scale parameters (x_0) for both fracture strength and tensile modulus followed the same trend as the mechanical parameters proving the feasibility of using Weibull analysis. x_0 showed an increasing trend from HT-15%PAN fiber to 15%PAN/1%CNT-3 fiber, while the HT-15%PAN/1%GNP-3 fiber showed the highest strengthening effects. However, GNPs and CNTs inclusion decreased the shape parameters (β) in strength, suggesting an increase in defect severity. As compared to the CNTs inclusion, PAN polymer chains filled the voids among planar graphene layers more easily than in the CNT networks due to the tube wall curvature. Modulus scale parameters (x_0) showed an equal value from HT-15%PAN fiber to 15%PAN/1%CNT-3 fiber, while the HT-15%PAN/1%GNP-3 fiber showed the highest stiffening effects. β showed an opposite trend to those of the strength value since the stiffness reinforcement is usually related to the nanoparticle alignment [46].

3.5. Polarized raman spectroscopy

Fig. 6(a) shows the cross-sectional SEM images of the 15%PAN/1%GNP-3 fiber with a zoomed-in section indicating the aligned GNP. To further study the spatial orientation of the GNPs, as well as proving the proposed mechanism in Fig. 5(c), polarized Raman spectroscopy was used. The G-band intensities of both materials under polarized Raman spectroscopy as a function of different incident angles have been previously studied to determine their orientations [47,48]. The middle and edge sections of the core GNP-containing layer were chosen as the laser incident spots, as shown in Fig. 6(b), while ϕ is the angle between the polarization direction and fiber axis. The optical images show the laser spots at ϕ =0° and 90° for the edge and middle sections.

Fig. $6(c_1 \text{ and } c_2)$ shows the corresponding responses at both the edge and middle of the fiber. When the laser was focused on the edge of the GNP layer, the intensity of the G-band (i.e., 1585 cm⁻¹) was smaller at $\phi = 90^{\circ}$ than that at $\phi = 0^{\circ}$ In comparison,

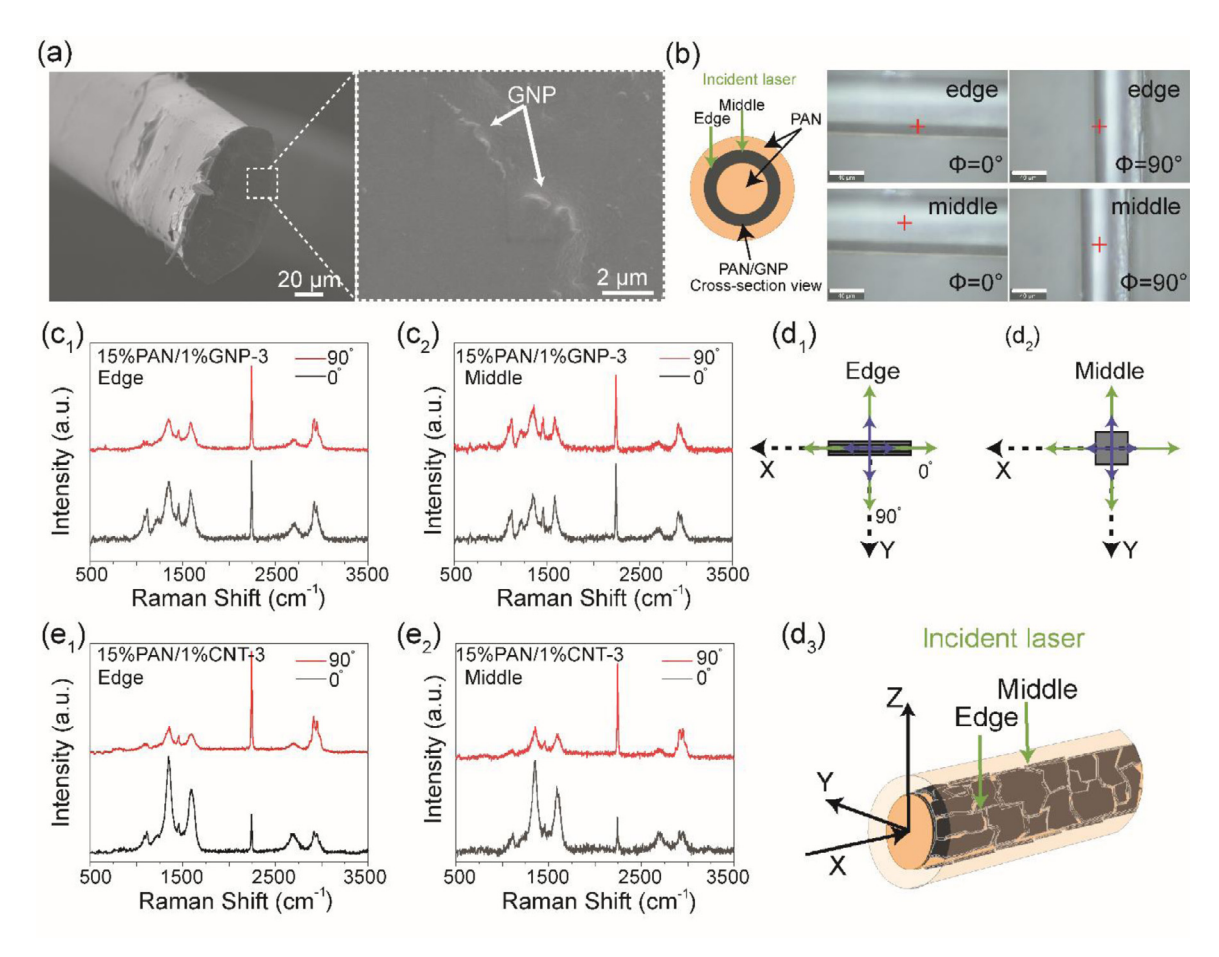


Fig. 6. Polarized Raman spectroscopy study on the orientation of GNPs and CNTs for the 3-layered structure. (a) Cross-sectional SEM images of the 15%PAN/1%GNP-3 with zoomed-in section showing aligned GNP. (b) Schematic showing the two Raman incident points on the middle and edge of the middle layer with optical images showing the rotation of 90° for both sections. The corresponding Raman signal for the edge and middle sections for (c_1, c_2) 15%PAN/1%GNP-3 and $(e_1 \text{ and } e_2)$ 15%PAN/1%CNT-3. (d_1-d_3) are the schematics for the orientations of GNP (For interpretation of the references to color in this figure, the reader is referred to the web version of this article.).

when the laser was focused on the middle of the fiber, the peak intensities remained the same regardless of ϕ angle. Schematics in Fig. $6(d_1$ and $d_2)$ show the concluded GNP orientation. The green arrows indicated the direction of the polarized laser, and the blue arrows showed the corresponding scattered radiation. The angular dependency for the fiber edge suggested that the 2D GNP was aligned along the x-axis (i.e., fiber axis) and was perpendicular to the y,z plane. The angular independence for the middle of the fiber suggested that the 2D GNP was parallel to the x-y plane. In sum, the orientation is shown in Fig. $6(d_3)$ where GNP nanoparticles were likely to be distributed in a concentric geometry with respect to the layers. This GNP morphology was highly consistent with the generation of shear stress across two different phases during the hot-drawing procedure, as previously mentioned.

As one-dimensional nanoparticles, CNTs would generate different spectra features from two-dimensional graphene depending on the incident point [42]. Fig. 6(e₁ and e₂) shows the polarized Raman spectra for the 15%PAN/1%CNT-3 fiber at both the edge and the middle sections with schematics showing the orientation of each case (Fig. S9 in the Supporting Information). Since G-band intensities showed strong angular dependency at both the edge and the middle of fiber and due to the 1D geometry, CNTs were expected to be aligned in the fiber axial direction.

3.6. Electrical properties for sensor applications

Pure PAN showed resistance beyond the testing capability of a multimeter; upon stabilization and carbonization, these fibers had a measured conductivity of 151.8 S/cm (Fig. 7(a)). The conductivity is between 12.5 to 20.0 S/cm for amorphous carbons, 200 to 300 S/cm for graphitic planes (parallel to the base plane), and 3.3 S/cm for graphitic planes (perpendicular to the base plane) [12]. As a comparison to these studies, the HT-15%PAN fibers may have formed continuous carbon pathways for the electrons to flow. The addition of GNPs and CNTs at 1 wt% (i.e., 15%PAN/1%GNP-3 and 15%PAN/1%CNT-3, respectively) did not exhibit any noticeable increase in their electrical conductivities before the heat-treatment, mainly due to not achieving required percolation thresholds. However, there were huge increases in conductivity after carbonization (i.e., HT-15%PAN/1%GNP-3 and HT-15%PAN/1%CNT-3, respectively), with the CNT containing fiber showing a more significant improvement (Fig. 7(a)). Experimentally, the intrinsic electrical conductivity can go as high as 10⁵ S/cm for a single CNT [49] and 10⁶ S/cm for a single layer of graphene [50]. However, theoretically, this electrical conductivity should not vary for graphitic layers, independent of the carbon forms, e.g., CNTs, graphene, or even graphitic CFs. In reality, it has been found that the number of stacked layers can influence electron flow capabilities, with the highest deterioration in CFs for the layer stacking or intertwining and the lowest decrease in CNTs due to its nanoscale effect [51]. This is consistent with our observation here that there is an increasing trend in conductivity from CFs to those containing GNPs

Electrically conductive carbons have been used widely in sensing materials, with a couple of demonstrations from our group [30,52]. In this study, a chemiresistive sensor based on HT-

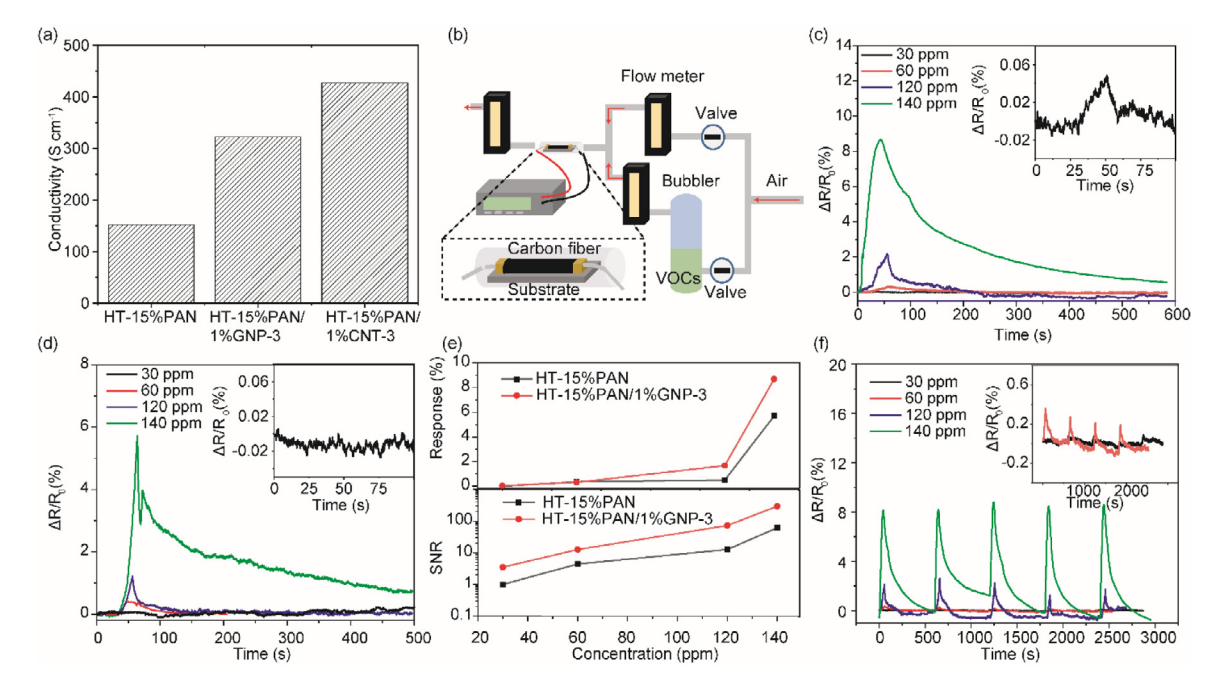


Fig. 7. Electrical and VOCs sensing performances. (a) The conductivity of three selected carbonized fibers at 1250 °C. (b) VOC sensing setup. Chemiresistive response of (c) HT-15%PAN/1%GNP-3 fiber and (d) HT-15%PAN fiber to various concentrations of methanol for 30 s. The zoomed-in sections are the response for 30 ppm concentration. (e) Response magnitude and their SNR with increasing concentrations for the two tested fibers. (f) The cyclical performance of the HT-15%PAN/1%GNP-3 fiber with various methanol concentrations.

15%PAN/1%GNP-3 fiber was demonstrated. Three fibers placed in parallel on a rigid substrate were put in a container and tested via an in-house designed sensing setup (Fig. 7(b)). A volatile organic compound (VOC) of methanol was chosen for the potential application of our fibers as biomarker sensors. According to the Occupational Safety and Health Administration (OSHA), methanol can be harmful to humans at concentrations over 200 ppm over prolonged periods of time [53]. Traditional solid-state VOC sensors often require a relatively high operating temperature due to their semi-conducting nature [54]. The ability to sense these VOCs at room temperature, as the fiber sensor from this study can do, is desired to reduce the operating costs. During the sensing tests, methanol vapors with concentrations ranging from 30 ppm, 60 ppm, 120 ppm, and 140 ppm, with a constant total flow of 300 ml/min, were maintained at room temperature (i.e., 25 °C). Both HT-15%PAN/1%GNP-3 and HT-15%PAN fibers were tested, and their responses were calculated based on $\Delta R/R_0$, where ΔR was the resistance change and R_0 was the initial resistance (Fig. 7(c,d)). With exposure to methanol vapor, an increase of resistance was expected due to the polar nature of methanol that could hinder the movement of charged electrons upon surface absorption [55]. HT-15%PAN/1%GNP-3 fiber showed a much higher response and a much larger signal-to-noise ratio (SNR) compared to the HT-15%PAN fiber (Fig. 7(e)). For 30 ppm concentration, 3-layered fiber showed an SNR of 3.5 while 1-phase fiber showed no distinct response (SNR = 1). This is likely due to the overall higher electrical conductivity induced by the embedded GNPs for the 3-layered fiber. Since the surface of the multilayered fiber and pure PANbased carbonized fiber had the same composition and morphology, the chemiresistive response was expected to be higher for lower R_0 of the HT-15%PAN/1%GNP-3 fiber. The cyclical performances of HT-15%PAN/1%GNP-3 fiber under various methanol concentrations are shown in Fig. 7(f). The highest concentration (i.e., 140 ppm) showed an average of 8% change in resistance, while the lowest concentration (i.e., 30 ppm) showed an average of 0.02% change in baseline resistance. The HT-15%PAN/1%GNP-3 fiber also responded to pressure changes caused by weight differences for deformation sensing applications, as demonstrated in Fig. S10 in the Supporting Information, for potential structural health monitoring of traditional laminated composites.

4. Conclusion

We reported the one-step fabrication of a new fiber microstructure containing multilayers. The interior-middle-exterior layer interactions rendered unique manipulation of nanoparticle morphologies and enabled much improved mechanical properties. It is critical to control the spinning dope compositions and the drawing conditions for effective graphene layers laminated between PAN channels during this manufacturing. The retained graphene planes tuned the carbon fiber properties in electrical and sensing performances, showing enormous potential in structural systems, in-situ health monitoring, environmental sustainability, and energy applications.

Data availability

The raw/processed data required to reproduce these findings cannot be shared at this time as the data also forms part of an ongoing study.

Declaration of Competing Interest

The authors declare that they have no known competing financial interests or personal relationships that could have appeared to influence the work reported in this paper.

Acknowledgment

This work is funded by the U.S. National Science Foundation (NSF, EAGER 1902172, 2019).

Supplementary materials

Supplementary material associated with this article can be found, in the online version, at doi:10.1016/j.jmst.2021.03.067.

References

- [1] M.S.A. Rahaman, A.F. Ismail, A. Mustafa, Polym. Degrad. Stab. 92 (2007) 1421-1432.
- [2] L. Penn, F. Larsen, J. Appl. Polym. Sci. 23 (1979) 59-73.
- [3] G. Srinivasan, D.H. Reneker, Polym. Int. 36 (1995) 195–201.
- [4] G.B. Kauffman, J. Chem. Educ. 70 (1993) 887-893.
- [5] G. Henrici-Olivé, S. Olivé, Adv. Polym. Sci. 51 (1983) 1-60.
- [6] B.J. Kim, Y. Eom, O. Kato, J. Miyawaki, B.C. Kim, I. Mochida, S.H. Yoon, Carbon NY. 77 (2014) 747-755.
- [7] Q. Wu, D. Pan, Text. Res. J. 72 (2002) 405-410.
- [8] Y. Zhang, K. Song, J. Meng, M.L. Minus, ACS Appl. Mater. Interfaces 5 (2013)
- [9] Y. Zhang, N. Tajaddod, K. Song, M.L. Minus, Carbon NY. 91 (2015) 479-493.
- [10] Y. Liu, S. Kumar, Polym. Rev. 52 (2012) 234–258.
- [11] B.A. Newcomb, Compos. Part A Appl. Sci. Manuf. 91 (2016) 262–282.
- [12] K. Song, Y. Zhang, J. Meng, E.C. Green, N. Tajaddod, H. Li, M.L. Minus, Materials 6 (2013) 2543–2577 Basel.
- [13] K. Song, R. Polak, D. Chen, M.F. Rubner, R.E. Cohen, K.A. Askar, ACS Appl. Mater. Interfaces 8 (2016) 20396-20406.
- [14] K. Song, D. Chen, K. Polak, M.F. Rubner, R.E. Cohen, K.A. Askar, ACS Appl. Mater. Interfaces 8 (2016) 35552-35564.
- [15] K. Song, Y. Zhang, M.L. Minus, Macromol. Chem. Phys. 216 (2015) 1313-1320.
- [16] H. Chang, M. Lu, J. Luo, J.G. Park, R. Liang, C. Park, S. Kumar, Carbon NY. 147 (2019) 419-426.
- [17] J. Cai, M. Naraghi, Acta Mater. 162 (2019) 46–54.
 [18] X. Zhang, H. Nguyen, M. Daly, S.B.T. Nguyen, H.D. Espinosa, Nanoscale 11 (2019) 12305-12316.
- [19] D. Papkov, N. Delpouve, L. Delbreilh, S. Araujo, T. Stockdale, S. Mamedov, K. Maleckis, Y. Zou, M.N. Andalib, E. Dargent, V.P. Dravid, M.V. Holt, C. Pellerin, Y.A. Dzenis, ACS Nano 13 (2019) 4893-4927.
- [20] K. Song, Y. Zhang, J. Meng, M.L. Minus, J. Appl. Polym. Sci. 127 (2013) 2977-2982.
- [21] W. Xu, D. Ravichandran, S. Jambhulkar, R. Franklin, Y. Zhu, K. Song, Adv. Mater. Technol. 5 (2020) 2000440.
- [22] Z. Gao, J. Zhu, S. Rajabpour, K. Joshi, M. Kowalik, B. Croom, Y. Schwab, L. Zhang, C. Bumgardner, K.R. Brown, D. Burden, J.W. Klett, A.C.T. Van Duin, L.V. Zhigilei, X. Li, Sci. Adv. 6 (2020) 1-11.
- [23] Q. Lu, M. Arroyo, R. Huang, J. Phys. D: Appl. Phys. 42 (2009) 102002.
- [24] C.Y. Hui, D. Shia, Polym. Eng. Sci. 38 (1998) 774-782.
- [25] X. Qian, X. Wang, J. Zhong, J. Zhi, F. Heng, Y. Zhang, S. Song, J. Raman Spectrosc. 50 (2019) 665-673.

- [26] M. Sekar, M. Pandiaraj, S. Bhansali, N. Ponpandian, C. Viswanathan, Sci. Rep. 9 (2019) 403.
- [27] B.K. Deka, A. Hazarika, J. Kim, N. Kim, H.E. Jeong, Y. Bin Park, H.W. Park, Chem. Eng. J. 355 (2019) 551-559.
- [28] N. Terasawa, I. Takeuchi, Electrochim. Acta 123 (2014) 340-345.
- [29] S. Yang, Z. Zhu, F. Wei, X. Yang, Build. Environ. 125 (2017) 60–66.
 [30] S. Jambhulkar, W. Xu, D. Ravichandran, J. Prakash, A. Nadar, M. Kannan, K. Song, Nano Lett. 20 (2020) 3199-3206.
- [31] W. Xu, S. Jambhulkar, R. Verma, R. Franklin, D. Ravichandran, K. Song, Nanoscale Adv. 1 (2019) 2510–2517.
- [32] S. Xiao, W. Cao, B. Wang, L. Xu, B. Chen, J. Appl. Polym. Sci. 127 (2013) 3198-3203.
- [33] H.E. Kissinger, Anal. Chem. 29 (1957) 1702-1706.
- [34] H. Chang, M. Lu, J. Luo, J.G. Park, R. Liang, C. Park, S. Kumar, Carbon NY. 147 (2019) 419-426.
- [35] J. Wang, L. Hu, C. Yang, W. Zhao, Y. Lu, RSC Adv. 6 (2016) 73404-73411.
- [36] M. Maghe, C. Creighton, L.C. Henderson, M.G. Huson, S. Nunna, S. Atkiss, N. Byrne, B.L. Fox, J. Mater. Chem. A 4 (2016) 16619–16626.
- [37] Z. Xu, C. Gao, Mater. Today 18 (2015) 480-492.
- [38] H.P. Cong, X.C. Ren, P. Wang, S.H. Yu, Sci. Rep. 2 (2012) 613.
 [39] S. Stankovich, D.A. Dikin, G.H.B. Dommett, K.M. Kohlhaas, E.J. Zimney, E.A. Stach, R.D. Piner, S.B.T. Nguyen, R.S. Ruoff, Nature 442 (2006) 282-286.
- [40] S.R. Ahmad, R.J. Young, I.A. Kinloch, Int. J. Chem. Eng. Appl. 6 (2015) 1-5.
- [41] A. Bisht, K. Dasgupta, D. Lahiri, J. Appl. Polym. Sci. 135 (2018) 1-11.
- [42] W. Xu, D. Ravichandran, S. Jambhulkar, Y. Zhu, K. Song, Adv. Funct. Mater. 31 (2021) 2009311.
- [43] G.C. Han, S. Kumar, Science 319 (2008) 908-909.
- [44] G. Sun, J.H.L. Pang, J. Zhou, Y. Zhang, Z. Zhan, L. Zheng, Appl. Phys. Lett. 101 (2012) 1905-1915.
- [45] B.W Weibull, J. Appl. Mech. 9 (1951) 293-297.
- [46] Y. Li, N. Mehra, T. Ji, X. Yang, L. Mu, J. Gu, J. Zhu, Nanoscale 10 (2018) 1695-1703
- Z. Li, R.J. Young, I.A. Kinloch, N.R. Wilson, A.J. Marsden, A.P.A. Raju, Carbon NY. 88 (2015) 215-224.
- [48] Q. Liang, X. Yao, W. Wang, Y. Liu, C.P. Wong, ACS Nano 5 (2011) 2392-2401.
- [49] T. Ebbesen, H. Lezec, H. Hiura, J. Bennett, H. Ghaemi, T. Thio, Nature 382 (1996) 54-56
- [50] X.Y. Fang, X.X. Yu, H.M. Zheng, H.B. Jin, L. Wang, M.S. Cao, Phys. Lett. A 379 (2015) 2245-2251.
- [51] B. Marinho, M. Ghislandi, E. Tkalya, C.E. Koning, G. de With, Powder Technol. 221 (2012) 351-358.
- [52] S. Jambhulkar, W. Xu, R. Franklin, D. Ravichandran, Y. Zhu, K. Song, J. Mater. Chem. C 8 (2020) 9495-9501.
- [53] J.E. Colman Lerner, E.Y. Sanchez, J.E. Sambeth, A.A. Porta, Atmos. Environ. 55 (2012) 440–447.
- [54] S.Y. Cho, H.W. Yoo, J.Y. Kim, W. Bin Jung, M.L. Jin, J.S. Kim, H.J. Jeon, H.T. Jung, Nano Lett. 16 (2016) 4508-4515
- [55] J. Wu, K. Tao, Y.Y. Guo, Z. Li, X.T. Wang, Z.Z. Luo, S.L. Feng, C.L. Du, D. Chen, J.M. Miao, L.K. Norford, Adv. Sci. 4 (2017) 1600319.